Bioinspiration &
Biomimetics

PAPER • **OPEN ACCESS**

Aerodynamic performance of autorotating seeds: scaling by size

To cite this article: Alberto Lolli *et al* 2026 *Bioinspir. Biomim.* **21** 026017

Bioinspiration & Biomimetics

PAPER

OPEN ACCESS

RECEIVED
11 July 2025

REVISED
23 December 2025

ACCEPTED FOR PUBLICATION
9 March 2026

PUBLISHED
16 April 2026

Aerodynamic performance of autorotating seeds: scaling by size

Alberto Lolli[1], **Giovanni Corsi**[1], **Barbara Mazzolai**[2] **and Antonio DeSimone**[1,3,*]

[1] The BioRobotics Institute, Scuola Superiore Sant'Anna, 56025 Pontedera, Italy
[2] Istituto Italiano di Tecnologia, 16163 Genova, Italy
[3] SISSA-International School for Advanced Studies, 34136 Trieste, Italy
[*] Author to whom any correspondence should be addressed.

E-mail: antonio.desimone@santannapisa.it and desimone@sissa.it

Keywords: computational fluid dynamics, winged seeds, auto-rotation

Supplementary material for this article is available online

Abstract

This study investigates the aerodynamics of a bio-inspired samara seed through high-fidelity numerical simulations, employing an overset mesh method to fully resolve its six-degree-of-freedom (6-DOF) motion. Coupled fluid and rigid body dynamics was solved using OpenFOAM v2406. A rigid 3D-printed seed prototype reproducing the samara of *Acer campestre* and its geometrically scaled versions (0.5x and 2x) were analyzed to explore the effects of scaling on passive flight dynamics. The simulations captured the full 6-DOF behavior, including the transition from uniformly accelerated vertical free-fall to steady autorotation. Key aerodynamic quantities such as descent velocity, angular velocity, coning and pitch angles, and the surrounding flow field structure were evaluated and compared. Simulation results are found to agree with scaling laws derived from the literature. Autorotation was found to be robust across scales, but strongly dependent on drop height and aerodynamic efficiency. The larger prototype (2x) exhibited the highest aerodynamic performance, while the small seed (0.5x) showed a reduced lift and, consequently, a comparatively higher descent velocity. Moreover, the 2x prototype, provided a greater surface area, thus offering potential functional benefits for applications to environmental sensing. Flow visualizations confirmed the formation of coherent leading-edge vortices, which contribute to lift generation and flight stability. The drop height necessary to establish steady autorotation increases with the size of the seed. These results suggest the existence of practical and biological limits for effective autorotational flight and offer design insights for passive bio-inspired flying systems that balance scalability, deployment constraints, and aerodynamic performance.

1. Introduction

Winged seeds, such as Samaras, exhibit a remarkable passive flight mechanism known as autorotation, where the seed spins around a vertical axis through the center of mass during its descent. This rotational motion induces aerodynamic forces that reduce the fall velocity of the seed, promoting greater dispersal distances over moderate lateral winds—an evolutionary adaptation that improves the survival of the species [1]. Although autorotation is the most commonly observed flight mode for samaras, it is not the only one: depending on geometry and mass distribution, winged seeds may also glide, while pappose seeds rely on parachute-like behavior for wind-driven transport [2, 3]. The transition between these flight modes is strongly controlled by the seed's center of mass location [4], which plays a decisive role in determining whether a stable autorotating descent or a tumbling/gliding motion emerges. Among these, Samaras from ash and elm trees often exhibit tumbling behavior during their spiral descent, while maple species prefer to autorotate around the vertical axis. In [5], it was shown that this stable behavior is retained by Samaras even after significant changes in their morphology, such as a 40% loss of the wing area or doubling of the weight. In these conditions, Samaras still trigger autorotation during flight and fall in a controlled descent. The natural samaras examined in these studies operate at Reynolds numbers on the order of 10^3, a regime in which thin disks of comparable size are known to exhibit chaotic

Figure 1. Photograph of the 3D-printed I-Sam [17] prototypes arranged in order of increasing scale factor (0.5x, 1x and 2x) from left to right.

or tumbling trajectories rather than a stable vertical fall [6–8]. This inherent stability and predictability of landing orientation make samara-type seeds particularly compelling as bioinspired platforms. A characteristic feature of their flight is the rapid transition from an initial near-vertical free fall to a tipping motion driven by asymmetric mass distribution, followed by the establishment of steady autorotation within less than a second [9]. Several numerical studies have modeled samara aerodynamics, though most focus on steady-state rotation or wind-tunnel-type inflow conditions [10, 11]. Other simulations investigate simplified geometries at Reynolds numbers significantly lower than natural values, and in some cases employ an imposed initial rotational velocity to trigger autorotation [12]. While informative, these assumptions alter or suppress the natural transient dynamics that is essential for our purpose. The interplay between fluid dynamics and seed morphology can be effectively studied with numerical simulations, as shown by Lee [13]. Such computational approaches prove particularly valuable when experimental measurement or direct visualization are challenging. From an engineering point of view, numerical models allow the comparison of seeds or designs of different sizes, facilitating the evaluation of their aerodynamic performance and optimization for bioinspired engineering applications in agritech [14], such as environmental sensing and reforestation. The development of passive aerial systems inspired by natural flyers, such as autorotating seeds, offers promising solutions for low-cost, low-energy deployment of small-scale devices for environmental sensing and precision agriculture, allowing data collection and seed deployment across large areas that may not be easily accessible [15, 16]. In this context, the design and optimization of bioinspired prototypes are crucial to achieve stable falling dynamics, ensuring landing with controlled velocities and orientation. Moreover, a key requirement for environmental sensing systems is to have a sufficiently large surface area to accommodate multiple sensors. These sensors are intended to be read wirelessly by aerial vehicles such as drones, hence the need to be oriented properly and visible from above [17]. However, enlarging the surface area by scaling up the prototype raises questions about whether the system would still retain its autorotating behavior and controlled descent. To address this question, we performed a numerical investigation on a reference prototype of autorotating seeds (based on the *Acer campestre*) presented in [17], which is produced by 3D printing. We simulated the falling motion of the seed as well as that of two geometrically scaled versions; see figure 1. These are obtained by scaling the geometry in all directions by a factor of 0.5 and 2, respectively. In the rest of the paper, we will refer to these 3 prototypes as 0.5x, 1x and 2x, where 1x indicates the original, non-rescaled geometry.

Our study is motivated by two main objectives: first, to determine the impact of geometric scaling on the aerodynamic performance and stability of the auto-rotation mechanism and, second, to identify the minimum drop height required to reliably trigger auto-rotation across different scales. Numerical simulations enable detailed analysis of the seed's descent trajectory and other key aerodynamic metrics, such as coning and pitch angles, angular velocity, and descent velocity. Furthermore, obtaining detailed visual insights into the structure of the fluid flow around the seed is valuable for the physical understanding of autorotational flight. An important example of such flow structures are the leading-edge vortices (LEVs) that form along the wing surface.

The remainder of this paper is organized as follows. Section 2 presents the mathematical modeling framework, including the aerodynamics of the seed, the dynamics of the fluid and the equations of motion of the seed coupled with the fluid. Section 3 reports the details on the numerical methods, model validation and the experimental settings for video recording and analysis. Section 4 reports the key results derived from simulations and experiments. In section 5, we summarize the main results and discuss the implications of our findings for seed dispersal of natural seeds and scalability of the design of artificial ones to be employed as environmental sensors.

2. Mathematical modeling

2.1. Seed aerodynamics: velocity and force components

In figure 2, three distinct reference frames are introduced to describe the kinematics and dynamics of the seed during its passive motion through air, following [12]. The first reference frame illustrated in figure 2 is the body frame, indicated as Σ_b, with origin in the center of mass and axes parallel to the principal axes of inertia of the seed. The second one is the geometric frame, denoted as Σ_g, and defined by the printing plane of the 3D model. This frame provides a geometric reference to illustrate the initial configuration of the prototype and its relationship with the orientation during printing, and is not used in the dynamic analysis of the motion of the seed. The first printed layer of the seed defines the 'geometric plane' (x_g, y_g) of Σ_g; subsequent layers are deposited sequentially along the direction normal to this plane, resulting in the gradual reconstruction of the full three-dimensional geometry. We define the geometric plane as the one normal to this direction of deposition passing through the center of mass of the seed. We identify the spanwise direction by projecting y_b on this plane; on this direction we define the axis y_g, extending from the center of mass to the wing tip. We then define the axis x_g orthogonal to both y_g and the direction of deposition, choosing the orientation from the thick (leading) edge to the thin (trailing) edge. Finally, the orientation of z_g (parallel to the direction of deposition, and thus perpendicular to the first layer) is chosen so that the resulting frame Σ_g is right-handed. Both Σ_g and Σ_b are fixed with respect to the seed. Lastly, the laboratory frame, denoted as Σ_{lab}, is an inertial frame fixed with respect to the external environment. In this frame, the vertical axis z_{lab} points opposite to the direction of gravity, and the horizontal plane is defined by $x_{lab}y_{lab}$. The position of the seed is defined by the coordinates of the center of mass with respect to Σ_{lab}, along with three Euler angles that describe the orientation of the body frame with respect to the laboratory. We adopt the roll-pitch-yaw convention, defining the coning (or roll) angle β, the pitch angle θ, and the yaw angle ψ. The angle β can be thought of as the angle generated during a rotation around the chordwise axis, while θ is generated by a rotation around the spanwise axis. They are represented in figure 3(a). At the initial time step Σ_g is aligned with the laboratory frame and then both angles β and θ are equal to 0. Once motion is initiated under the action of gravity, the seed begins to rotate around its own x_b-axis due to the lack of symmetry of its mass distribution. As a result, the seed deviates from the horizontal plane: the angle between the y_b-axis of the body frame and its projection on the horizontal plane is the coning angle. The pitch angle instead is measured as the angle between x_b and its projection on the horizontal plane. The geometry of the problem is illustrated schematically in figure 3. In this figure, we dropped the distinction between the body and geometric frame since their axes are very close. The section plane represented in the left panel contains the axis of auto-rotation and the direction of y_g: we have assumed the axis of autorotation to coincide with z_{lab}. This approximation is supported by numerical results: in figure 6, where the trajectories of the falling motions of the seeds are shown, lateral displacements do not exceed 1% of the vertical component. Therefore, the view on the left is on a plane with normal vector that lies on the horizontal plane $x_{lab}y_{lab}$. The view on the right panel of figure 3 is instead in a plane orthogonal to the spanwise direction (and thus to y_g), which we denote as chordwise section. In such a geometric Section, one can naturally introduce the lift and drag forces generated by the aerodynamics of the seed motion, thus justifying the introduction of the geometric frame. During descent, the seed experiences a resultant velocity [18] defined as $v_{res} = \sqrt{v_{dn}^2 + v_{tan}^2} = \cos(\beta)\sqrt{v_d^2 + \omega^2 r^2}$. This vector couples the effects of the vertical (falling) velocity v_d with the rotational velocity ω, see figure 3 for the definition of the components. The angle formed between v_{res} and v_{tan} defines the gliding angle, given by $\epsilon = \tan^{-1}\left(\frac{v_{dn}}{v_{tan}}\right)$. It is important to note that the gliding angle (which is directly related to the angle of attack [19]) varies along the span, as a result of variations in the tangential velocity v_{tan}; see figure 8. The aerodynamic force acting on the wing is decomposed into two components: the drag D, aligned with v_{res}, and its normal counterpart, the lift L (figure 3(b)). The resultant aerodynamic force balances the normal component of the weight, $\frac{W}{\cos\beta}$, as shown in figure 3(a). The coning angle on which the autorotation settles is determined by the equilibrium of the opposing moments, about the center of mass, of

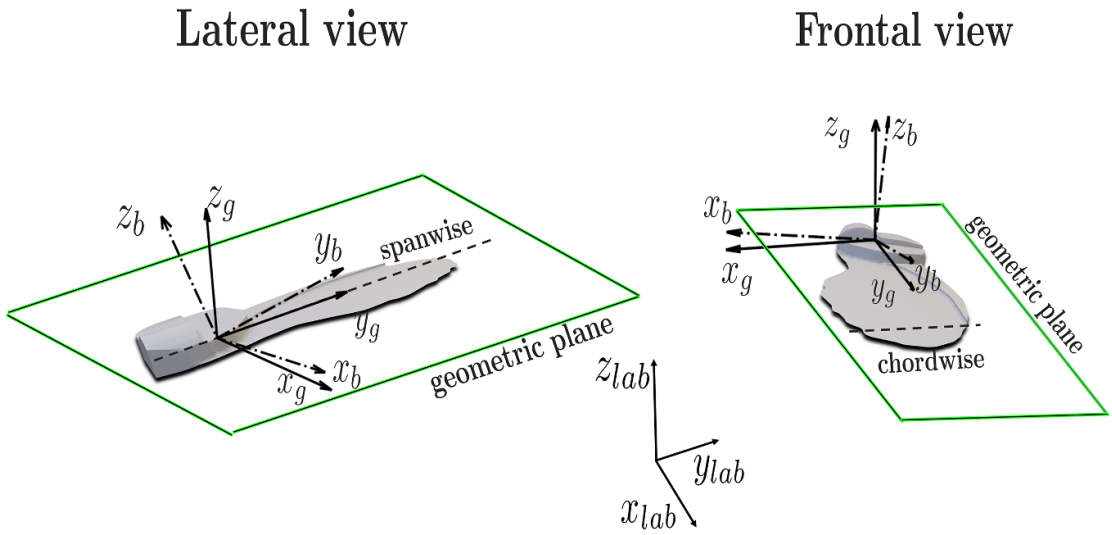

Figure 2. I-Sam prototype designed in [17]. Axes $\{x_{\text{lab}}, y_{\text{lab}}, z_{\text{lab}}\}$ define the inertial laboratory frame Σ_{lab}, while axes of the Σ_{b} and Σ_{g} frames define the body frame and the geometric one.

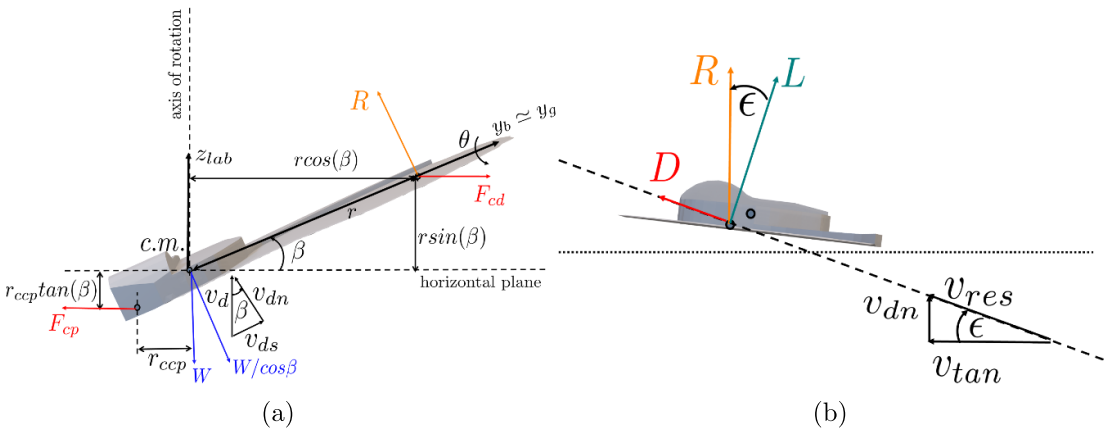

Figure 3. Illustration of the sectional views: (a) Spanwise and (b) Chordwise, showing the aerodynamic forces, velocity components, and angles governing the motion.

the centrifugal (F_{cd} and F_{cp}) in figure 3(a) and aerodynamic forces.

2.2. Fluid dynamics

We simulated the falling motion in quiescent air, treating the fluid as incompressible due to the low Mach number regime. We solve directly the incompressible Navier–Stokes equations (without using turbulence models), below expressed in index notation where $i,j = 1,2,3$ identify the components with respect to the axes of the lab frame Σ_{lab}:

$$\begin{cases} \frac{\partial v_i}{\partial x_i} = 0 \\ \rho\left(\frac{\partial v_i}{\partial t} + v_j \frac{\partial v_i}{\partial x_j}\right) = -\frac{\partial p}{\partial x_i} + \mu \frac{\partial}{\partial x_j}\left(\frac{\partial v_i}{\partial x_j} + \frac{\partial v_j}{\partial x_i}\right) + f_i \end{cases} . \tag{1}$$

v_i, p are the ith component of the velocity and pressure fields, $f_i = \rho g_i$ represent the gravity force per unit volume, $\rho = 1.225 \frac{\text{kg}}{\text{m}^3}$ is the fluid density and μ its dynamic viscosity, of value $\mu = 1.81 \times 10^{-5}\text{Pa}\cdot\text{s}$ at 20°. The fluid force **F** and moment **M** acting on the seed are calculated by integrating the contributions of pressure and viscous stresses on the surface of the body, denoted by $\partial\mathcal{B}$. These quantities are expressed component-wise in Σ_{lab} as follows:

$$\begin{cases} F_i = \int_{\partial\mathcal{B}} \left(\mu D_{ij} - p\delta_{ij}\right) n_j \, \mathrm{d}\Sigma \\ M_i = \int_{\partial\mathcal{B}} \left(r_j \times \left(\mu D_{ij} - p\delta_{ij}\right) n_j\right) \mathrm{d}\Sigma \end{cases} \tag{2}$$

where tensor D_{ij} represents the symmetric part of the velocity gradient $\frac{\partial v_i}{\partial x_j}$, r_j the components of the vector joining the force application point and the moment center (the center of mass), and n_j the components of the normal to the seed's surface.

Table 1. Geometrical and mass properties of the three simulated prototypes. The inertia tensor is measured in Σ_b.

	I-Sam 0.5x	I-Sam 1x	I-Sam 2x
m (kg)	6.9×10^{-06}	5.5×10^{-05}	4.4×10^{-04}
r_{span} (m)	1.4×10^{-02}	2.9×10^{-02}	5.8×10^{-02}
A_{seed} (m^2)	1.3554×10^{-04}	5.4218×10^{-04}	2.1687×10^{-03}
A_{wing} (m^2)	8.4903×10^{-05}	3.3963×10^{-04}	1.3586×10^{-03}
V (m^3)	1.65×10^{-08}	1.32×10^{-07}	1.06×10^{-06}
J_{xx} ($kg \cdot m^2$)	1.7986×10^{-10}	1.7440×10^{-09}	5.6280×10^{-08}
J_{yy} ($kg \cdot m^2$)	3.2391×10^{-11}	3.1607×10^{-10}	1.0135×10^{-08}
J_{zz} ($kg \cdot m^2$)	2.0886×10^{-10}	2.0270×10^{-09}	6.5355×10^{-08}

2.3. Equations of motion

The evolution over time of the six degrees of freedom of the rigid-body dynamics of the seed is governed by the Newton–Euler equations. The motion of the center of gravity is expressed in the laboratory frame Σ_{lab}, see figure 2:

$$m\dot{\mathbf{v}}_{cm} = \mathbf{W} + \mathbf{F}, \tag{3}$$

where m is the body mass, $\mathbf{W}$ is the weight of the seed, corrected to take into account the buoyancy force and $\mathbf{F}$ is the aerodynamic force. The angular motion of the object instead is computed in the body frame Σ_b, illustrated again in figure 2, by solving

$$\mathbb{J}\dot{\boldsymbol{\omega}} + \boldsymbol{\omega} \times (\mathbb{J}\boldsymbol{\omega}) = \mathbf{M} \tag{4}$$

where $\boldsymbol{\omega}$ is the angular velocity vector and $\mathbf{M}$ is the moment of the aerodynamic forces. The inertia tensor $\mathbb{J}$ is diagonal since the body frame is aligned with the principal axes. The components of this tensor are reported in table 1, together with other geometrical parameters. Since (4) is solved in the body frame, the evolution in time of the relative orientation between the body and laboratory frames must be known. To avoid singularities which can arise during the resolution of the rotational dynamics using Euler angles, quaternions $\mathbb{Q} = (Q_1, Q_2, Q_3, Q_4)$ are employed:

$$\begin{cases} Q_i = e_i \sin\left(\frac{\phi}{2}\right) & \forall i = 1,2,3 \\ Q_4 = \cos\left(\frac{\phi}{2}\right) \end{cases} \tag{5}$$

which describe a rotation of an angle ϕ about an axis with unit vector of components e_i. The evolution in time of the quaternions is given by:

$$\frac{d\mathbb{Q}}{dt} = \frac{1}{2}\begin{bmatrix} 0 & \omega_z & -\omega_y & \omega_x \\ -\omega_z & 0 & \omega_x & \omega_y \\ \omega_y & -\omega_x & 0 & \omega_z \\ -\omega_x & -\omega_y & -\omega_z & 0 \end{bmatrix} \mathbb{Q} \tag{6}$$

where $(\omega_x, \omega_y, \omega_z)$ are the components of the angular velocity vector in the body frame.

3. Methods

3.1. Numerical methods & model validation

Simulating the complex dynamic motion of the seed over time involves the solution of a fluid-structure interaction (FSI) problem, on a moving/deforming domain. In our case, we employ the overset mesh method [20, 21]. In this approach, two meshes are combined: one, the component mesh, is body-fitted to the boundary of the seed and follows its motion, and is sufficiently refined to accurately capture the flow features close to the body. The second, less refined, is the background mesh, and comprises the entire region of the motion. Boundary information is exchanged between these grids through interpolation of the flow variables, which is crucial for accurately resolving the relative motion between the seed and the surrounding air. The coupled FSI problem governing the falling seed dynamics is solved through an iterative algorithm using OpenFOAM-v2406 [22] and a full flowchart illustrating the sequence of the calculations is represented in figure 4. The governing equations are discretized in both time and space, and coupling between the fluid flow and the rigid body motion is obtained in two steps: the fluid dynamics are resolved using the PIMPLE algorithm [23], maintaining the Courant–Friedrichs–Lewy number below 2. Then, the Newton–Euler equations of the rigid motion are updated with the fluid forces at each new time step and advanced in time using a Symplectic solver. The equations of the fluid are discretized in space with the finite volume method. An example of the computational domain of one of the simulations is illustrated in figure 5 and reported in table 4, and consists of an assembled mesh of approximately 900 000 hexahedral cells, with a refinement in the inner part of the body-fitted zone. Parameters such as the aspect ratio, skewness and orthogonality of the cells are checked to ensure a good quality mesh in all simulated cases. We also conducted a preliminary check of the stability of our results with respect to mesh refinement (see table in appendix). Given the complexity of the geometry of the seed and the small size of its finest features, performing a more detailed analysis would be worthwhile but is left for further studies. A no-slip velocity boundary condition is enforced on the surface of the seed. A zero-velocity condition is applied at the outer domain walls, with the exception of the upper side (with respect to the direction of gravity), where a zero-pressure condition is assigned to allow natural fluid outflow. For discretization in time, the Crank–Nicolson scheme, with a blending factor of 0.5, is applied, ensuring second-order accuracy. The gradient terms, including pressure and velocity gradients, are approximated using a Gauss linear scheme. The advection of momentum is discretized using a *linearUpwind* (second order)

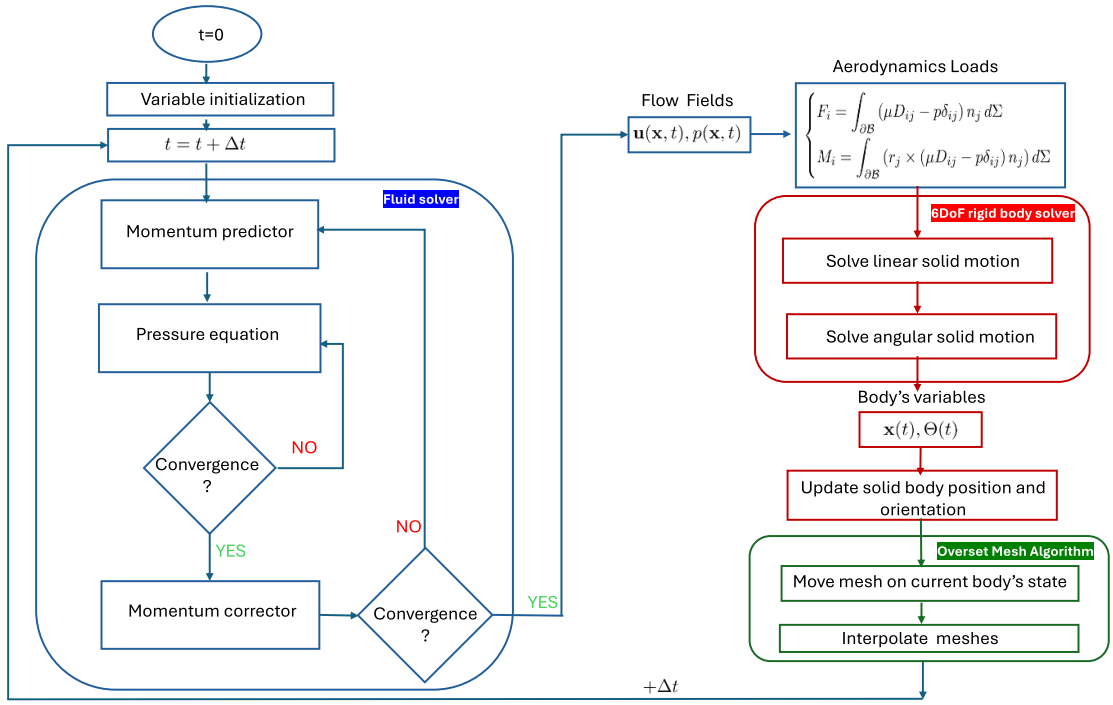

Figure 4. Schematic representation of the Fluid Structure Interaction algorithm.

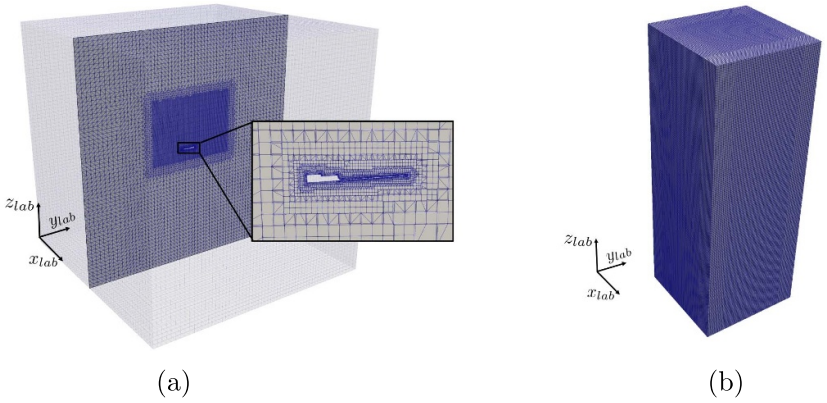

Figure 5. Visualization of the component (a) and background (b) mesh zones. The component zone is a cubic domain; a section plane highlights the refined wake region around the seed, including a zoomed-in view. The background zone is a larger parallelepiped domain encompassing the entire computational region.

divergence scheme. Viscous and diffusive terms are approximated with a limited Gauss linear scheme.

The accuracy and reliability of the proposed model were validated against benchmark cases from the literature, incorporating both computational and experimental data. In particular, the results reported by Uhlmann [24] were reproduced, showing good agreement with their findings. The case considered is that of a solid sphere falling in an unbounded, quiescent fluid, under the effect of gravity. The solid to fluid density ratio was set to 2.56 (heavier solid) for both cases. Two different Reynolds number regimes (computed with respect to the steady state value of the falling velocity, U_∞) were tested, by varying the kinematic viscosity of the fluid. The motion reaches a steady terminal velocity over time in both cases. The results, compared with experiments 1 and 2 from section 5.3 of [24], are presented quantitatively in table 2 , respectively. For further validation, we reproduced results from [25], for the case of the buoyancy-driven motion of disks. We focused on the case of a disk with aspect ratio $\chi = 2$, and density ratio $\frac{\rho_s}{\rho_f} = 0.99$. The resulting Galileo number was $G = 160$, and the motion unsteady. Once a limit cycle was reached, we calculated the average falling velocity, comparing it with the one reported in the reference, see table 3.

Table 2. Comparison of Reynolds numbers at steady-state $Re_\infty = U_\infty D/\nu$ between our model and the benchmark data from [24].

Cases	Uhlmann	Our model	Relative error
1)Re_∞	41.12	41.31	0.4%
2)Re_∞	366.69	372.54	1.5%

Table 3. Comparison of Reynolds numbers at steady-state $Re_\infty = U_\infty D/\nu$. between our model and the benchmark data from [25].

	Chrust *et al*	Our model	Relative error
Re_∞	242	247	2.1%

Table 4. Computational domain characteristics for the component and background zones.

	Component zone	Background zone
Cells number	500.000	400.000
Cells type	Hexahedra	Hexahedra
Domain height (m)	0.2	2.5
Domain length (m)	0.2	0.5

The simulation results are in good agreement with reference data for all the tested scenarios.

3.2. Experimental recording

The 3D-printed artificial seeds, illustrated in figure 1, were manufactured at Istituto Italiano di Tecnologia. The infill density of the nut was set to 5%, while that of the wing was set to 100%. The achieved layer thickness of 0.05 mm for the wing corresponds to the minimum resolution limit of the employed 3D printer (Prusa i3 MK3S). High-speed videos of the falling seeds were recorded using a Photron high-speed camera. For the 0.5x and 1x scale seeds, recordings were made at 500 frames per second (fps), while for the 2x scale seeds the frame rate was increased to 750 fps to better capture the faster motion. Each seed was released from an initial height of 3.5 m and allowed to fall freely in quiescent air, with at least three repetitions performed for each sample. The temporal scale of the recorded videos was determined directly from the inverse of the camera frame rate, a known acquisition parameter of the setup. The spatial scale was calibrated using an A4 sheet of paper (29.7 cm $\times$ 21.0 cm) placed in the same plane as the falling seed and visible within the field of view. Using the Tracker calibration tool, a line was drawn along the long edge of the sheet (29.7 cm) and used as the reference distance, enabling pixel-to-length conversion. The seed position was manually tracked frame-by-frame by marking its centroid using Tracker [26], an open-source motion analysis tool. Instantaneous velocities were obtained via finite differences between consecutive frames. To reduce noise and transient effects, velocities were averaged over the last 20 frames, corresponding to the steady-state regime of the motion. Since the motion develops predominantly along the vertical direction and the perspective effects were minimal, the recorded velocities represent an approximate estimate of the vertical descent speed. These values were reported in table 5 for qualitative comparison with numerical results, but were not used for quantitative validation of the simulations. Video '1x FullFlight.mp4' shows the complete free-fall flight of the 1x prototype, from the moment of release to the onset and stabilization of autorotation. The same experiment is shown in 2x FullFlight.mp4', but referring to the 2x prototype. To isolate the steady-state phase, three separate recordings, '0.5x SteadyFlight.mp4', '1x SteadyFlight.mp4' and '2x SteadyFlight.mp4', were captured. These videos provide a clearer depiction of both the transient and limit-cycle dynamics of the falling seed, offering visual confirmation of the behaviors observed in the numerical results, see figures 11, 10. One can clearly observe the transition from the initial phase of uniformly accelerated vertical free-fall to the onset of autorotation accompanied by a sudden deceleration of the descent velocity. Finally, '2x SteadyNumerical.mp4' shows the numerical counterpart of the 2x seed falling in its steady regime, with the evolution of the fluid velocity field through contour and quiver plots to indicate the magnitude and direction of the flow. This last video is made in ParaView [27].

4. Results

Results are reported for the three prototypes, with the aim of: (i) identifying the minimum release height required to trigger autorotation, (ii) evaluating aerodynamic efficiency, and (iii) analyzing vortex structures along the spanwise and chordwise directions. Finally, we examine the entire descent flight through the time evolution of the velocity and attitude of the seed. Each seed is initially released from rest at the origin of the computational domain, with gravity acting as the only external force, directed downward as $\mathbf{g} = (0, 0, -9.81\frac{\mathrm{m}}{\mathrm{s}^2})$. Each simulation was run for a time sufficient to observe the onset of autorotation and the convergence of the motion to a limit cycle. Figure 6(a) illustrates the trajectories of the centers of mass in the laboratory frame, while Figure 6(b) shows their projections onto the horizontal plane over the full simulation time. It is evident that the larger prototype achieves a greater dispersal distance, whereas the 0.5x and 1x descend predominantly along the vertical axis. The falling height before triggering of autorotation, denoted as h_{drop}, is reported for each prototype in table 7, together with the corresponding average

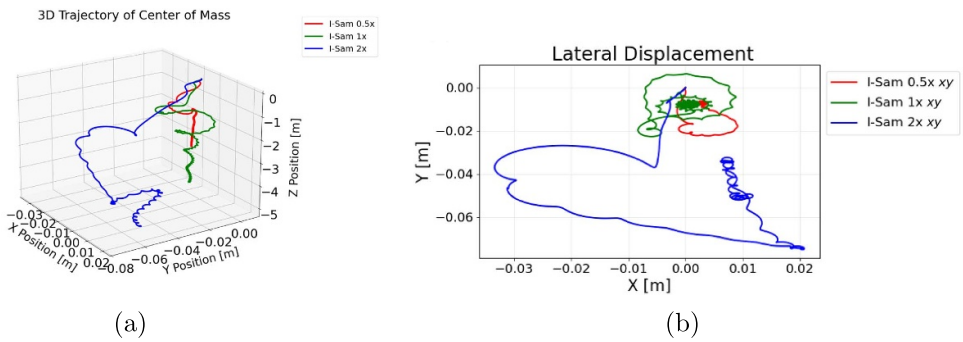

Figure 6. Trajectories of the center of mass. (a) 3D evolution. (b) Projected displacement in the horizontal plane.

steady-state coning and pitch angles. In table 8 we present the descent velocities of the numerically simulated prototypes, which lie within the experimentally measured confidence intervals reported in table 6. The weight of the real 3D-printed seeds may differ from that of the numerical prototypes, which strictly follow the scaling laws relating weight and dimensions. For this reason, the prototypes reported in tables 7 and 8 are labeled differently. Specifically, table 7 refers to the prototypes presented by [17], while table 8 reports the properties of the seeds used in this work to produce the experimental videos. These latter prototypes were fabricated using the same 3D printing procedure as in [17], but at a later time.

Following [28], we define the descent factor D_f as

$$D_f = \frac{2W}{\rho_f v_d^2 A}. \tag{7}$$

This dimensionless parameter is often used to quantify the aerodynamic efficiency of the seed. In steady state conditions, the weight force is absorbed by two aerodynamic contributions (one generated by the vertical fall speed v_d and one by rotation, which generates additional upward thrust). The descent factor represents the ratio between the weight of the body and the first aerodynamic contribution (aerodynamic drag). When the descent factor is greater than one, it means that the first contribution is less than the weight, so the seed is able to compensate for the difference through the contribution made by rotation. The higher the DF, the more important this contribution is, which is why we quantify aerodynamic efficiency in this way. Our results demonstrate that autorotation is successfully triggered for all three prototypes. The 2x prototype exhibits the highest aerodynamic efficiency, as indicated by a higher value of D_f, followed by the 1x and 0.5x. The small prototype shows the worst performance, with a reduced descent factor, suggesting a diminished lift contribution from autorotation.

Table 5. Experimental mass and descent velocity for the three prototypes (0.5x, 1x, 2x) use for the videos presented in section 3.2.

	$\tilde{I}-$ Sam 0.5x	$\tilde{I}-$ Sam 1x	$\tilde{I}-$ Sam 2x
m (kg)	1.7×10^{-05}	1.03×10^{-04}	6.6×10^{-04}
v_d (m s^{-1})	1.5	1.45	2

Table 6. Experimental vertical descent, angular, and tip velocities for the three Samara seed prototypes (0.5x, 1x, 2x) reported in the supplementary materials of [17].

	$I-$ Sam 0.5x	$I-$ Sam 1x	$I-$ Sam 2x
m (kg)	1.12×10^{-05}	5.5×10^{-05}	5.99×10^{-04}
v_d (m s^{-1})	0.97 ± 0.09	1.04 ± 0.09	1.82 ± 0.33
ω_z (rad s^{-1})	161.1 ± 36.9	107.1 ± 16.7	68.3 ± 6.3
v_{tip} (m s^{-1})	2.04 ± 0.53	2.64 ± 0.41	3.50 ± 0.39

Table 7. Numerical results of the minimum required h_{drop}, descent factor and averaged steady state coning and pitch angles.

	I-Sam 0.5x	I-Sam 1x	I-Sam 2x
h_{drop} (m)	0.95	1.5	3.2
D_f	2	2.70	3
β (deg)	25.15	23.5	23.2
θ (deg)	-4.04	-3.11	-2.90

Table 8. Numerical results: velocities are time-averaged over the last 0.5 s of steady state motion.

	I-Sam 0.5x	I-Sam 1x	I-Sam 2x
m (kg)	6.9×10^{-06}	5.5×10^{-05}	4.4×10^{-04}
v_d (m s^{-1})	-0.79	-0.98	-1.3
ω_z (rad s^{-1})	132	98	70
v_{tip} (m s^{-1})	1.3	2.1	3.1

A striking feature of natural autorotating seeds is their aerodynamic robustness to morphological variations, such as changes in the wing area or mass distribution [5]. We analyze the effect of scaling on the performance analytically. In the literature, the seed's descent velocity $\mathbf{v}_d$ is commonly correlated with wing loading—defined as the ratio of seed weight **W**

Table 9. Numerical results of time-averaged fluid forces over the last 0.5 s of steady state motion, expressed in the lab frame Σ_{lab}.

	I-Sam 0.5x	I-Sam 1x	I-Sam 2x
W (N)	6.77×10^{-05}	5.399×10^{-04}	4.34×10^{-03}
F_x (N)	5.07×10^{-07}	-5.12×10^{-06}	-6.90×10^{-05}
F_y (N)	-7.67×10^{-07}	-2.412×10^{-06}	-1.74×10^{-05}
F_z (N)	6.77×10^{-05}	5.39×10^{-04}	4.37×10^{-03}
M_x (Nm)	2.60×10^{-06}	-1.57×10^{-05}	-3.12×10^{-04}
M_y (Nm)	-1.77×10^{-06}	5.97×10^{-06}	2.88×10^{-04}
M_z (Nm)	1.89×10^{-09}	-4.35×10^{-08}	-3.28×10^{-06}
Re_∞	1e+03	2e+03	6.5e+03

to its wing area A—according to the relationship:

$$\rho_{\text{f}} \mathbf{v}_{\text{d}}^2 \sim \frac{\mathbf{W}}{A}. \tag{8}$$

The weight of the object scales with the cube of the scaling factor λ. Indeed

$$\mathbf{W} = \rho_{\text{s}} \mathbf{g} V \implies \mathbf{W}_\lambda = \rho_{\text{s}} \mathbf{g} \lambda^3 L^3 = \lambda^3 \mathbf{W}, \tag{9}$$

where ρ_{s} represents the seed density, $\mathbf{g}$ the gravity force vector and V the volume of the seed and $L = V^{1/3}$ is the characteristic length; while the scaling law for the area A is given by

$$A \sim L^2 \implies A_\lambda = \lambda^2 L^2. \tag{10}$$

Using the scaling factor λ in equations (7*a*) and (7*b*) of [29], we obtain:

$$\begin{cases} v_{\text{d},\lambda} \propto \sqrt{\lambda} v_{\text{d}} \\ \omega_\lambda \propto \dfrac{1}{\sqrt{\lambda}} \omega \end{cases}. \tag{11}$$

We plot these relations and the data-points from numerical results in figure 7. The curves are positioned so that the values for $\lambda = 1$ are the descent velocity and rotation rate calculated in the numerical simulation of the 1x prototype. Figure 7(a) illustrates the vertical descent velocity as a function of the scale factor. The red curve represents the theoretical trend predicted by the square-root scaling law (11), while the green square markers correspond to the results of the numerical simulations for the three seed prototypes (see table 8). In figure 7(b), the same is done for the angular velocity. The numerical results show the same trends of the theoretical prediction based on the scaling law, and the agreement is particularly good for the rotation velocities. The larger seeds exhibit lower angular velocities. While this agreement should be interpreted only in a qualitative sense, the resulting interpolating functions provide an approximate but interesting means of estimating descent and rotational velocities for seeds with sizes contained in the range of those actually simulated, thereby alleviating the burden of simulating individually prototypes at intermediate scales.

According to both experiments and theory, the descent velocity increases with the scaling factor. All the measured falling speeds of the tested prototypes align well with theoretical expectations. Figure 8(a) shows the tangential velocity distribution along the spanwise coordinate for all three prototypes. It is shown that the tangential velocity of the smaller seed is the lowest, despite its rotational velocity being the highest. This supports the fact that its descent factor is also the lowest and hence the 0.5x prototype is the one with the lowest aerodynamic efficiency. Figure 8(b) depicts the distribution of the gliding angle along the seed span, which confirms its inverse relationship with the tangential velocity, as defined in section 2.1. It is noteworthy that the 0.5x prototype exhibits higher tip gliding angles than the 1x and 2x seeds, which attain stable autorotation at lower gliding angles, indicative of improved aerodynamic performance. A critical aerodynamic feature influencing seed descent is the formation of LEVs, which enhance lift by maintaining attached flow even at high angles of attack [28]. Previous studies [30] have demonstrated that LEVs play a vital role in biological flyers like insects and bats and remain stable even at relatively low Reynolds numbers ($Re \approx 120$) for flapping wings. We observe that LEVs are stable for all the prototypes we examined. However, we see in figures 9(e)–(f) a weakening of the LEV structures for the larger 2x one, where the Reynolds number attains the largest value in the order of $6.5 \cdot 10^3$. This is reminiscent of the observation of vortex bursting at Reynolds $> 10^3$ contained in [31]. Here, the authors suggest that this vortex bursting does not produce a diminished aerodynamic performance, a fact which may explain the increment in the descent factor which we observe for the larger samaras.

The analysis of the velocity field, presented in figure 9, reveals the emergence of coherent vortex structures along both the spanwise and chordwise directions of the seed for all scaled prototypes. These vortices form as the seed rotates and its leading edge interacts with the incoming flow, generating a recirculation region that accelerates the flow near the wing surface, thereby inducing a localized low-pressure zone. It is important to note that the aerodynamic efficiency of the seed decreases with increasing gliding angle, as higher angles tend to produce less compact LEVs.

Finally, we show the time evolution of the coning angle $\beta(t)$ and pitch angle $\theta(t)$ in figure 10, and of the linear and angular velocity components in figure 11. As previously mentioned, the seed initially lies on the horizontal plane, corresponding to β, $\theta = 0$. At release, a rotational motion around the seed's x-axis is triggered by gravity due to the non-symmetric mass distribution. Within approximately 0.15 s, the seed undergoes a significant change in the coning angle

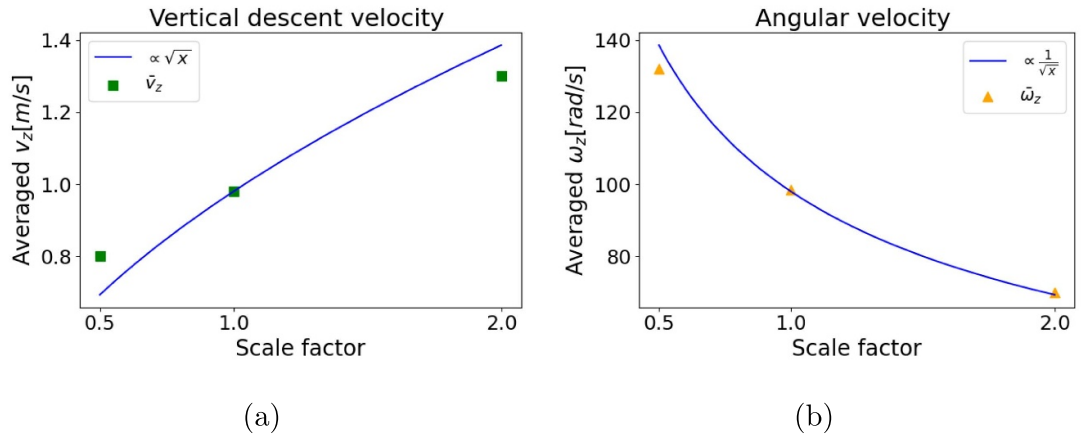

Figure 7. Scaling laws (11) of the velocities: (a) Mean descent velocity as a function of the scaling factor. (b) Mean angular velocity as a function of the scaling factor.

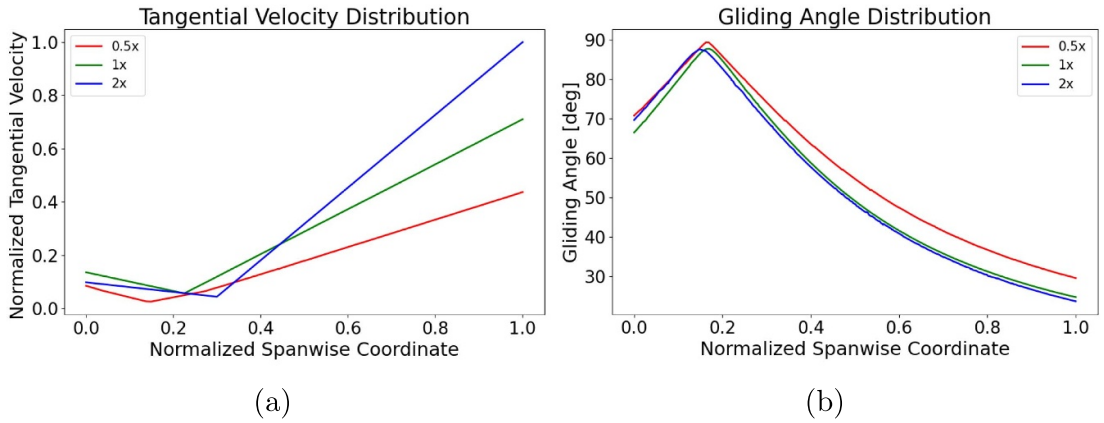

Figure 8. Distribution of aerodynamic variables along the spanwise direction: (a) tangential velocity and (b) gliding angle.

with the wing tip tilting upwards, resulting in a configuration where the projected area facing the flow is minimal. Consequently, aerodynamic forces are insufficient to counteract gravity, and the seed accelerates. This orientation is maintained until approximately 0.45 s for the 0.5x and 1x prototypes, and up to 0.75 s for the 2x prototype. Figures 10 and 11 represent the entire evolution of the seed's dynamics: time series of the components of linear and angular velocity, and of the coning and pitch angles are reported. The colored vertical bars mark the transition from an almost uniformly accelerated vertical descent to the onset of autorotation for all three prototypes respectively. At this transition point the seed starts to autorotate and there is a marked reduction in both the coning angle and vertical descent velocity, which quickly converge towards (essentially) steady-state values, after a vertical fall of height h_{drop}. We refer to the final part of the motion as the steady state, characterized by minimal temporal variations in the observed quantities. The time-averaged terminal values over the last 0.5 s of motion are reported in tables 7, 8 and 9. The videos and the whole set of results discussed above underscore the inherently nonlinear nature of falling seed dynamics, particularly highlighting the transition from an initial transient regime of uniformly accelerated vertical free-fall to a steady autorotation mode. Furthermore, we note that the overall motion predominantly develops around the vertical z-axis, demonstrating the effectiveness of the auto-rotation mechanism in establishing a slow descent along a preferred direction, with a controlled landing orientation.

5. Discussion

The numerical framework used in this study allowed us to simulate the complex unsteady aerodynamics of auto-rotating seeds. The model was first validated against benchmark cases, demonstrating good agreement in all scenarios. By scaling the size of the seed and analyzing key aerodynamic quantities, we explored how geometric scaling influences

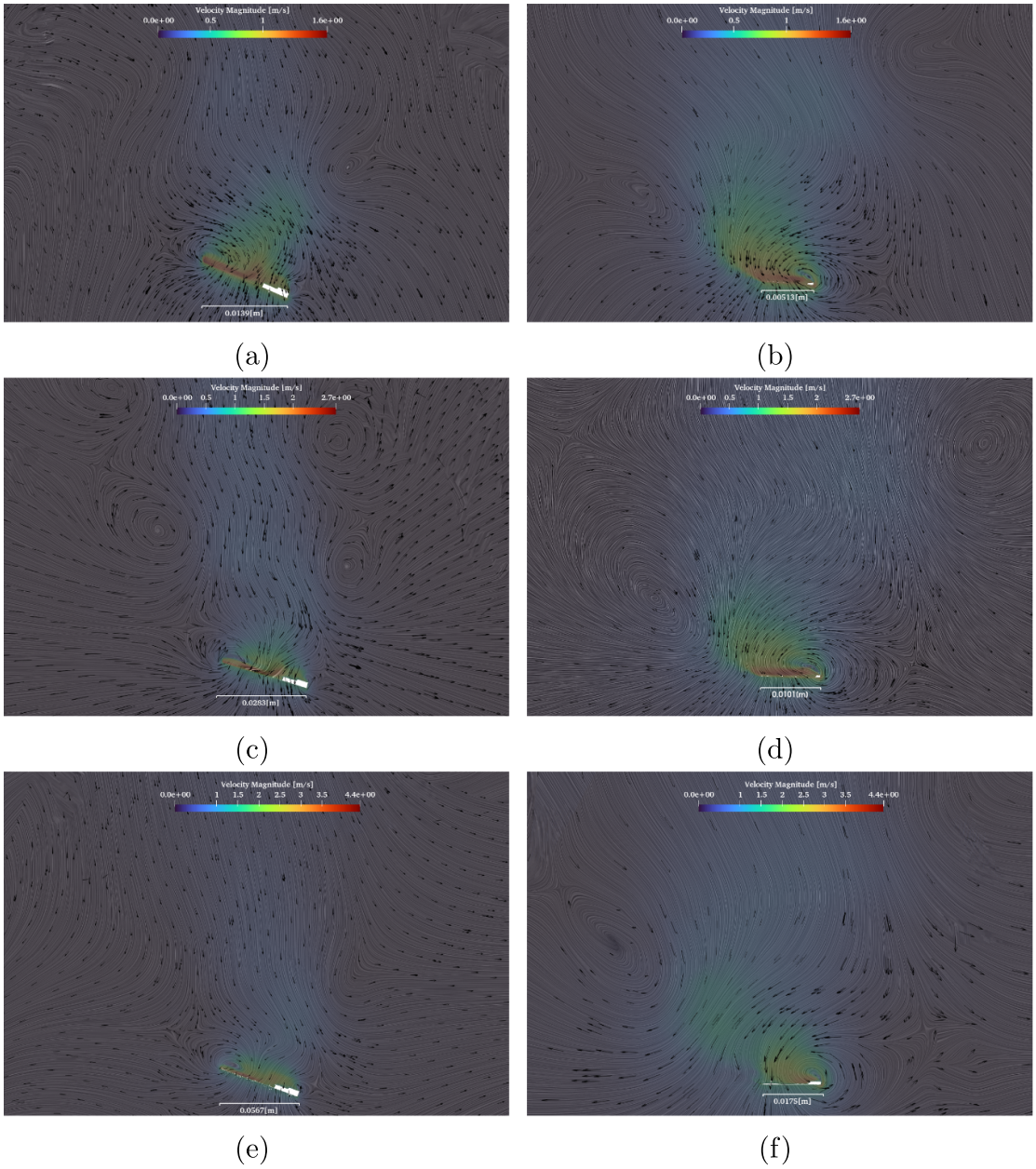

Figure 9. Spanwise (a), (c), (e) and chordwise (b), (d), (f) velocity fields for the 0.5x, 1x, and 2x I-Sam prototypes during autorotation. The colormap indicates velocity magnitude, quivers show flow direction, and the horizontal scalebar denotes the local spanwise/chordwise coordinate radius.

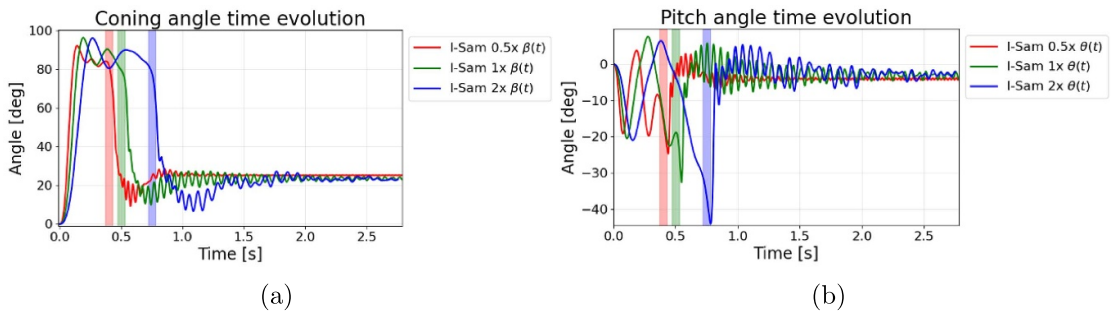

Figure 10. (a) Time evolution of the coning and (b) time evolution of the pitch angle over the simulation period.

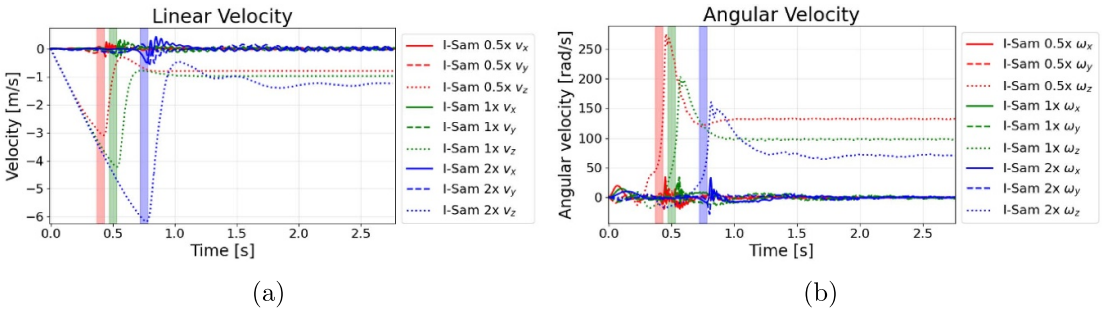

Figure 11. (a) Time evolution of the linear velocities and (b) time evolution of the angular velocities over the simulation period.

the autorotational performance of Samara-inspired seeds, both natural and artificial. Our results show that stable autorotation can be achieved across a range of scales, confirming the robustness of this passive flight mode. All tested prototypes were able to initiate autorotation, but the height required to trigger this mechanism increases significantly with scale. This is a potential problem for our intended use cases, where rapid deployment and efficient dispersion from low altitudes are essential. The 0.5x prototype, on the other hand, fails to significantly reduce its descent velocity, possibly compromising the ability to disperse under moderate lateral winds. The biological implication of this behavior is that seeds that are too small may not be transported far from the parent tree, causing them to land nearby and increase competition for survival. Among all designs, the 2x prototype demonstrated the highest aerodynamic efficiency, making it the optimal choice in terms of performance. Furthermore, it offers compelling advantages from an engineering perspective in applications such as environmental sensing [15–17]. Its larger surface area, four times that of the 1x prototype, provides more space for sensor and payload integration. Moreover, its larger physical dimensions enhance detectability, facilitating localization and recovery in field applications. The presence and compactness of LEVs are crucial for maintaining flow attachment, this aerodynamic mechanism enhances lift and promotes dynamic stability during autorotation [28]. Our analysis of the velocity field (see figure 9) confirms that such vortex structures form consistently for all three prototypes, both along the spanwise and chordwise directions. Notably, the persistence of these LEVs despite changes in geometry suggests that their formation is robust to scaling, thereby supporting sustained autorotation over a wide range of seed sizes. This observation is consistent with previous findings in [5], which highlight the ability of various autorotating seeds to maintain autorotation in a variety of sizes and morphologies. The findings suggest the existence of a critical size threshold beyond which aerodynamic performance begins to degrade. The small prototype appears to fall faster than expected, potentially due to insufficient lift generated through autorotation, as indicated by lower values of the descent factor D_f, and lower values of the attained tangential velocity (see figure 8(a). These observations are consistent with the idea that the autorotation mechanism could lose effectiveness below a certain geometric scale. Interestingly, in nature, the smallest autorotating seeds tend to be larger than the 0.5x prototype considered here, which may hint at a biological lower bound for effective passive autorotational flight. From an engineering point of view, printing at scaling factors below 0.5x presents challenges due to the reduced thickness of the wing and to potential problems for its structural integrity. These constraints may also contribute to the explanation of why a lower bound for the size of autorotating seeds is observed in nature. Compared to the other prototypes, the 2x design showed superior aerodynamic efficiency, emerging as the most effective configuration overall. With regard to the upper size limit, we scaled the prototype up to three times its original size and observed that the minimum falling height required to initiate autorotation increased significantly, reaching approximately 7 m. This requirement may pose practical limitations for applications, as it requires deployment from substantial heights. This is also in line with biological observations, where large autorotating seeds are relatively rare. The scarcity of such seeds in nature may be attributed to the prolonged transient phase and increased drop height needed to achieve stable autorotation. Consequently, only trees exceeding the critical drop height, h_{drop}, would benefit from dispersal strategies based on autorotation. We hope that our findings may contribute to a deeper understanding of how autorotational behavior scales with size and to inform the design of effective bio-inspired devices where passive flight, sensing, and deployment constraints must be carefully balanced.

6. Conclusions

In this work, we investigated the aerodynamics of geometrically scaled samara seeds through fully coupled 6-DOF numerical simulations using an overset mesh framework. Our results demonstrate that autorotation is a remarkably robust passive flight strategy, consistently triggered across all tested scales. We highlight how geometric scaling affects the autorotational performance, with implications for engineering and natural seed dispersal. From an engineering perspective, aerodynamic efficiency and performance as environmental sensing are both monotone increasing with size, making larger prototypes more effective in carrying payloads and providing stable descent speed. However, the height required to establish autorotation also grows monotonically with scale, potentially limiting deployability in real environments where strong lateral gusts or insufficient release altitude may disrupt the onset of autorotation. This trade-off points to the existence of an upper practical size for bio-inspired environmental sensors. At the other end of the spectrum, very small designs face manufacturing challenges (thin wings become structurally fragile) and show reduced aerodynamic efficiency, indicating a lower bound on feasible miniaturization. These observations mirror patterns found in natural samaras, which occupy a relatively narrow size window across species. The analysis suggests that this biological range may arise from the same competing constraints: seeds that are too small would lose aerodynamic effectiveness and structural robustness, whereas overly large seeds would require drop heights attainable only by the tallest trees to reliably trigger autorotation. In this light, both natural evolution and engineering design appear governed by a balance between aerodynamic performance, material limitations, and deployment constraints, which together define an optimal intermediate size for effective autorotational flight.

Acknowledgment

This project has received funding from the European Union's Horizon 2020 research and innovation program under Grant Agreement No. 101017940 (I-Seed). We also gratefully acknowledge support by the Italian Ministry of University and Research (MUR) through #NEXTGENERATIONEU (NGEU), National Recovery and Resilience Plan (NRRP), project THE (IECS00000017) - Tuscany Health Ecosystem (DN. 1553 11.10.2022), and PRIN projects 2020/PFCXPE—Response, control and learning: building new manipulation strategies in living and engineered active matter, 2022/ABYSS: Accurate simulation of Bio-hYbrid Soft Swimmers. The authors thank Rouwen Tu for the 3D printing of the seeds used for the free fall videos. We also wish to acknowledge valuable scientific discussions with Jacopo Quaglierini and Anna Chiara Bressi. We acknowledge the EuroHPC Joint Undertaking for awarding this project access to the EuroHPC supercomputer LEONARDO, hosted by CINECA (Italy) and the LEONARDO consortium through an EuroHPC Regular Access call. We acknowledge the EuroHPC Joint Undertaking for awarding this project access to the EuroHPC supercomputer LUMI, hosted by CSC (Finland) and the LUMI consortium through a EuroHPC Regular Access call.

Data availability statement

All data that support the findings of this study are included within the article (and any supplementary files).

1x Experimental Full Flight Video available at https://doi.org/10.1088/1748-3190/ae4f46/data1.

2x Experimental Full Flight Video available at https://doi.org/10.1088/1748-3190/ae4f46/data2.

0.5x Experimental Steady Flight available at https://doi.org/10.1088/1748-3190/ae4f46/data3.

1x Experimental Steady Flight available at https://doi.org/10.1088/1748-3190/ae4f46/data4.

2x Experimental Steady Flight available at https://doi.org/10.1088/1748-3190/ae4f46/data5.

2x Numerical Steady Flight available at https://doi.org/10.1088/1748-3190/ae4f46/data6.

Seed attitude time evolution Video available at https://doi.org/10.1088/1748-3190/ae4f46/data7.

Author contributions

Alberto Lolli 0009-0008-9227-774X
Conceptualization (equal), Data curation (equal), Investigation (equal), Methodology (equal), Software (equal), Validation (equal), Visualization (equal), Writing – original draft (equal), Writing – review & editing (equal)

Giovanni Corsi 0000-0002-4535-1803
Investigation (equal), Software (equal), Supervision (equal), Validation (equal), Writing – original draft (equal), Writing – review & editing (equal)

Barbara Mazzolai 0000-0003-0722-8350
Funding acquisition (equal), Project administration (equal), Writing – review & editing (supporting)

Antonio DeSimone 0000-0002-2632-3057
Conceptualization (equal), Funding acquisition (equal), Project administration (equal), Resources (equal), Supervision (equal), Methodology (equal), Validation (equal), Writing – review & editing (equal)

Table A1. Grid convergence study for the 1x prototype.

	Coarse mesh	Current mesh	Fine mesh
No. of cells	500.000	900.000	1.800.000
F_z [N]	5.39×10^{-04}	5.39×10^{-04}	5.40×10^{-04}
β [deg]	23.7	23.5	23.5
θ [deg]	−3.09	−3.11	−3.21
ω_z [rad s^{-1}]	9.80e+01	9.82e+01	9.79e+01
v_z [m s^{-1}]	-9.84×10^{-01}	-9.75×10^{-01}	-9.76×10^{-01}

Appendix

To assess the numerical accuracy and grid independence of the proposed computational framework, a grid convergence study was performed for the 1x prototype. Three different mesh resolutions: coarse, current, and fine were considered, while keeping all physical and numerical parameters unchanged. Key aerodynamic and kinematic quantities, including vertical force, descent velocity, angular velocity, and attitude angles, were evaluated once the steady autorotational regime was reached. The results reported in table A1 show negligible variations across mesh resolutions, indicating that the adopted mesh provides a satisfactory compromise between accuracy and computational cost and that the numerical results presented in this work are effectively grid independent.

References

[1] Nathan R, Katul G G, Horn H S, Thomas S M, Oren R, Avissar R, Pacala S W and Levin S A 2002 Mechanisms of long-distance dispersal of seeds by wind *Nature* **418** 409–13

[2] Minami S and Azuma A 2003 Various flying modes of wind-dispersal seeds *J. Theor. Biol.* **225** 1–14

[3] Cummins C, Seale M, Macente A, Certini D, Mastropaolo E, Viola I M and Nakayama N 2018 A separated vortex ring underlies the flight of the dandelion *Nature* **562** 414–8

[4] Hou Z-B, Zhang J-D, Yun-Da Li, Jia Y-X and Huang W-Xi 2025 Aerodynamic significance of mass distribution on diverse samara descent behaviors *Commun. Eng.* **4** 129

[5] Schaeffer B M, Truman S S and Truscott T T *et al* 2024 Maple samara flight is robust to morphological perturbation and united by a classic drag model *Commun. Biol.* **7** 248

[6] Field S B, Klaus M, Moore M G and Nori F 1997 Chaotic dynamics of falling disks *Nature* **388** 252–4

[7] Tinklenberg A, Guala M and Coletti F 2023 Thin disks falling in air *J. Fluid Mech.* **962** A3

[8] Corsi G, Ledda P G, Vagnoli G, Gallaire F and De Simone A 2024 Instability and trajectories of buoyancy-driven annular disks: a numerical study *Phys. Rev. Fluids* **9** 043907

[9] Varshney K, Chang S and Wang Z J 2011 The kinematics of falling maple seeds and the initial transition to a helical motion *Nonlinearity* **25** C1

[10] Zakaria M Y *et al* 2019 Modeling and prediction of aerodynamic characteristics of free fall rotating wing based on experiments *Int. Conf. on Aerospace Sciences and Aviation Technology* vol 18 pp 1–15

[11] Chen T and Lan S 2022 Numerical analysis of dynamic stability of falling maple samaras *Acta Mech. Sin.* **38** 322111

[12] Arranz G, Moriche M, Uhlmann M, Flores O and García-Villalba M 2018 Kinematics and dynamics of the autorotation of a model winged seed *Bioinspir. Biomim.* **13** 036011

[13] Lee I 2016 Numerical study of a freely-falling maple seed *PhD Thesis*

[14] Jung B and Rezgui D 2017 Investigating the autorotational performance of scaled samara rotor in vertical and forward flight *42nd European Rotorcraft Forum 2016* (Association Aeronautique et Astronautique de France) pp 1252–66

[15] Mazzolai B, Kraus T, Pirrone N, Kooistra L, De Simone A, Cottin A and Margheri L 2021 Towards new frontiers for distributed environmental monitoring based on an ecosystem of plant seed-like soft robots *Proc. Conf. on Information Technology for Social Good* pp 221–4

[16] Mazzolai B, Kraus T, Pirrone N, Kooistra L, De Simone A, Cottin A and Margheri L 2022 Advancing environmental intelligence through novel approaches in soft bioinspired robotics and allied technologies: I-seed project position paper for environmental intelligence in europe *Proc. of the 2022 ACM Conf. on Information Technology for Social Good* pp 265–8

[17] Cikalleshi K, Nexha A, Kister T, Ronzan M, Mondini A, Mariani S, Kraus T and Mazzolai B 2023 A printed luminescent flier inspired by plant seeds for eco-friendly physical sensing *Sci. Adv.* **9** eadi8492

[18] Åke Norberg R 1973 Autorotation, self-stability and structure of single-winged fruits and seeds (samaras) with comparative remarks on animal flight *Biol. Rev.* **48** 561–96

[19] Lee S J, Lee E J and Sohn M H 2014 Mechanism of autorotation flight of maple samaras (acer palmatum) *Exp. Fluids* **55** 1–9

[20] Chandar D D and Gopalan H 2016 Comparative analysis of the arbitrary mesh interface (ami) and overset methods for dynamic body motions in openfoam *46th AIAA Fluid Dynamics Conf.* p 3324

[21] Koomullil R, Cheng G, Soni B, Noack R and Prewitt N 2008 Moving-body simulations using overset framework with rigid body dynamics *Math. Comput. Simul.* **78** 618–26

[22] Foundation O 2024 *Openfoam User Guide* (ESI-OpenCFD Ltd) (https:// www.openfoam.com/documentation)

[23] Oliveira P J and Issa R I 2001 An improved piso algorithm for the computation of buoyancy-driven flows *Numer. Heat Transfer B-Fund.* **40** 473–93

[24] Uhlmann M 2005 An immersed boundary method with direct forcing for the simulation of particulate flows *J. Comput. Phys.* **209** 448–76

[25] Chrust M, Bouchet G and Dušek J 2013 Numerical simulation of the dynamics of freely falling discs *Phys. Fluids* **25** 044102

[26] Brown D 2023 Tracker video analysis and modeling tool (https://physlets.org/tracker/) (Version 6.1.5, Open Source Physics)

[27] Ayachit U 2015 *The Paraview Guide: a Parallel Visualization Application* (Kitware, Inc)

[28] Lentink D, Dickson W B, Van Leeuwen J L and Dickinson M H 2009 Leading-edge vortices elevate lift of autorotating plant seeds *Science* **324** 1438–40

[29] Azuma A and Yasuda K 1989 Flight performance of rotary seeds *J. Theor. Biol.* **138** 23–53

[30] Harbig R R, Sheridan J and Thompson M C 2013 Reynolds number and aspect ratio effects on the leading-edge vortex for rotating insect wing planforms *J. Fluid Mech.* **717** 166–92

[31] Lentink D and Dickinson M H 2009 Rotational accelerations stabilize leading edge vortices on revolving fly wings *J. Exp. Biol.* **212** 2705–19